Sustainable Carbon Materials

https://doi.org/10.48130/scm-0026-0010

Original Research

Open Access

Co-upcycling of polyurethane and biomass for synthesizing functionalized N-doped hierarchical porous carbon for high-performance aqueous zinc-ion hybrid capacitors

Guanyu Zhang, Tianqi Cao, Zengjian Guo, Xuesong Zhang* and Lujia Han

Received: 11 December 2025

Revised: 21 January 2026

Accepted: 26 January 2026

Published online: 10 March 2026

Abstract

Aqueous Zn-ion hybrid capacitors (ZIHCs) are promising next-generation energy storage devices that combine high energy density with high power density. However, current carbon cathodes with a suboptimal porous structure do not match the zinc anode, especially hindering the transportation and storage of $(Zn[H_2O]_6)^{2+}$, resulting in low energy density and poor cycling durability. To address this challenge, nitrogen-doped hierarchical porous carbons (NHPCs) have emerged as a promising cathode material. Conventional synthesis of NHPCs relies on costly and environmentally harmful nitrogen sources (e.g., cyanides, amines), hindering sustainable production. Herein, functionalized carbonaceous materials were synthesized using biomass and nitrogen-rich plastic waste (polyurethane, PU) as precursors through carbonization followed by activation. The obtained N-3@AC-4 (with a biomass to PU ratio of 3:1 and activator to carbon precursor ratio of 4:1) achieved a remarkable specific capacitance of 430.6 F g^{-1}, at a current density of 0.1 A g^{-1} in a typical three-electrode system. When configured into ZIHCs, N-3@AC-4 maintained a high specific capacitance of 356.9 F g^{-1}, at the same current density, coupled with a superior energy density of 126.89 Wh kg^{-1}, at a power density of 80 W kg^{-1}. Furthermore, the device demonstrated long cycling stability, with ~85% capacitance retention after 5,000 cycles. Overall, this study presented a sustainable and effective strategy for synthesizing advanced carbonaceous cathode materials for high-performance aqueous ZIHCs.

Keywords: Aqueous zinc-ion hybrid capacitors, Nitrogen-doped hierarchical porous carbons, Polyurethane, Biomass, Integrated fabrications, Exceptional Zn storage capability

Highlights

- Functionalized NHPCs are synthesized through the co-processing of biomass and polyurethane.
- NHPCs possessed a well-developed 3D-interconnected porous structure (> 1,100 m^2 g^{-1}).
- N-3@AC-4 in ZIHCs exhibited a remarkable energy density (126.89 Wh kg^{-1} at 80 W kg^{-1}).
- N-3@AC-4 in ZIHCs showed excellent cycling stability (~85%) over 5,000 cycles.

* Correspondence: Xuesong Zhang (xszhang@cau.edu.cn)

Full list of author information is available at the end of the article.

https://doi.org/10.48130/scm-0026-0010

Graphical abstract

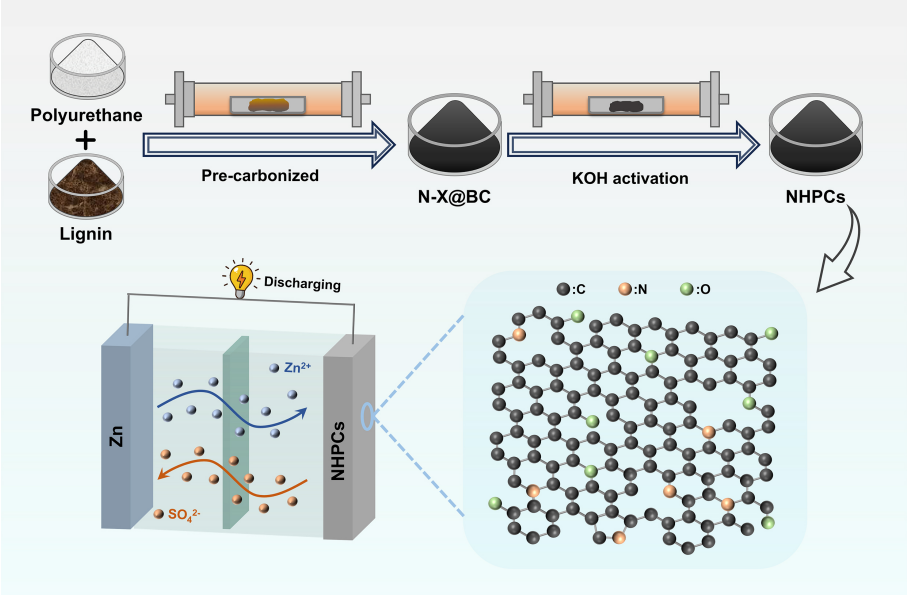

Introduction

The rapid development of renewable energy offers a promising solution to mitigate fossil fuel depletion and environmental pollution[1,2]. However, their inherent intermittency and multi-time-scale random fluctuations pose a significant challenge to grid stability[3]. To address this instability, electrochemical energy storage systems have gained significant attention for balancing electricity supply and demand[4,5]. Among various electrochemical energy storage systems, lithium-ion batteries (LIBs) and supercapacitors (SCs) have been extensively developed and applied[6]. Unfortunately, the complementary yet insufficient characteristics of LIBs, (high energy density and low power density) and SCs (high power density, long cycle life, and low energy density) limit their broader application[7,8]. In response to these limitations, Zn-ion hybrid capacitors (ZIHCs) have emerged as a next-generation energy storage device, attracting interest due to their potential for combining sustainability, high specific power, energy density, and long cycle life[9,10]. Additionally, owing to the use of non-flammable aqueous electrolytes, aqueous ZIHCs exhibit superior safety and are more environmentally friendly than organic batteries[11].

Despite the compelling advantages of metallic zinc anodes, such as high theoretical specific capacity (823 mAh g^{-1}) and natural abundance[12,13], the overall performance of ZIHCs is often constrained by the limited energy density of conventional cathode materials[14,15]. To address this cathode-induced performance bottleneck, numerous studies have been dedicated to developing advanced carbon materials with optimized physicochemical properties[16,17]. In this context, biomass-derived carbon materials have emerged as a compelling candidate for advanced cathodes, owing to their sustainability, cost-effectiveness, eco-friendliness, as well as their tunable pore structures and surface chemistry[18–21].

The electrochemical performance of a carbon-based cathode is critically governed by three key parameters: its specific surface area, pore distribution, and surface functional groups[6]. Electrodes fabricated from high specific surface area carbonaceous materials facilitate efficient storage and release of Zn^{2+} ions, resulting in the enhancement of both energy and power density in ZISCs[22]. Owing to its high specific surface area and low cost, commercial activated carbon (AC) has been employed as a cathode material for ZIHCs[23]. However, the performance of AC is often constrained by its inherent limitations. Its pore structure is typically dominated by micropores (≤ 2 nm), which hinders the rapid diffusion of hydrated Zn^{2+} ions ($[Zn(H_2O)_6]^{2+}$, with a kinetic diameter of ~0.86 nm)[24]. More importantly, due to its low content of heteroatoms, AC primarily relies on the electrical double-layer capacitance (EDLC) mechanism for energy storage, which results in a low energy density[25].

The incorporation of heteroatoms is a pervasive strategy to enhance the electrochemical performance of carbonaceous materials[26,27]. N-doping can effectively optimize the pore structure, improve surface wettability, increase charge density, and induce lattice distortion to create abundant active sites of carbonaceous materials[28]. This modification collectively contributes to significantly enhanced ions adsorption capacity and charge storage capabilities[29]. However, conventional nitrogen sources for synthesizing N-doped hierarchical porous carbon (NHPCs), such as cyanides, amines, and other N-containing organics are often costly, unsustainable and environmentally harmful, which poses significant challenges for large-scale green manufacturing[30–32]. In this context, utilizing nitrogen-rich waste resources as alternative precursors has emerged as a promising and sustainable pathway for preparing high-performance carbon materials[33–35]. Polyurethane (PU) foam stands out as a particularly compelling candidate among various waste streams, owing to its status as a widely used polymer with an annual production exceeding 15 million metric tons and its inherent richness in nitrogen atoms[36]. The substantial consumption of PU inevitably leads to the generation of massive post-industrial and post-consumer waste, necessitating efficient recycling and upcycling strategies[37,38]. Therefore, the design and synthesis of NHPCs derived from waste PU and biomass offer a dual advantage: addressing the environmental issues of plastic and biomass waste while providing a sustainable and cost-effective nitrogen source for preparing high-performance cathodes for ZIHCs[39,40].

Herein, a novel and sustainable strategy for synthesizing NHPCs from the co-processing of biomass and PU for ZIHCs is presented. The optimized N-doped carbonaceous material (N-3@AC-4) exhibited exceptional electrochemical performance, achieving a high specific capacitance of 430.6 F g^{-1} at a current density of 0.1 A g^{-1} in a three-electrode system, and maintaining 356.9 F g^{-1} in ZIHCs at the same current density, coupled with a superior energy density of 126.89 Wh kg^{-1} at a power density of 80 W kg^{-1}. Overall, this work establishes a feasible route for co-upcycling biomass and PU waste into advanced carbonaceous materials for high-performance ZIHCs, offering a promising solution for the development of energy storage and the promotion of a circular economy.

Materials and methods

Materials and chemicals

The biomass feedstocks used in this work, including reed (RD), corn stover (CS), and pine sawdust (PS), were collected from agricultural and forestry sources. The obtained biomass was pulverized into 100 mesh and then washed with deionized (DI) water to remove surface dust. Thereafter, it was placed in an oven to dry at 105 °C overnight for further use. Polyurethane (PU) was obtained from Huachuang Plastic Ltd., China. Dealkalized lignin (DL), ethanol, KOH, and $ZnSO_4 \cdot 7H_2O$ were purchased from Macklin.

Preparation of nitrogen-doped hierarchical porous carbons (NHPCs)

Biomass species and PU were mixed and ground uniformly with a mass ratio of 1:1–1:4. The precursor was pre-carbonized at 800 °C for 2 h at the heating rate of 10 °C min^{-1} in a tube furnace with continued argon flow. After cooling to room temperature, the obtained carbonaceous material was washed with DI water and then dried at 105 °C overnight. The precursors were termed as N-X@BC, where X (= 1, 2, 3, 4) represents the mass ratio of PU to biomass source. After that, N-X@BC and KOH with suitable mass ratio (1:3–1:5) were dissolved in DI water, followed by stirring for 12 h. The dried mixture was activated at 800 °C for 2 h with a heating rate of 10 °C min^{-1} and then cooled to ambient temperature. Finally, the carbonaceous material was thoroughly washed with DI water until it reached neutrality before being stored for subsequent tests. The obtained NHPCs were termed as N-X@AC-Y or N-X@AC-Z, where X (= 1, 2, 3, 4) represents the mass ratio of PU to biomass source, Y (= 3, 4, 5) represents the mass ratio of KOH to N-X@BC, and Z (= CS, DL, RD, PS) represents the biomass sources.

Structure characterization

Morphologies of carbonaceous materials were observed by scanning electron microscopy (SEM). The crystal structures of the samples was investigated using X-ray diffractometers (XRD). The functional groups of NHPCs were investigated by Fourier transform infrared (FTIR) analysis. The porous characteristics were measured by N_2 adsorption-desorption analysis. The elemental compositions and distributions of the elements in NHPCs were investigated by energy-dispersive X-ray spectroscopy (EDS). The surface chemical states of carbonaceous materials were assessed by X-ray photoelectron spectroscopy (XPS). The crystallinity and graphitization degree were characterized by Raman analysis.

Electrochemical characterization

Electrode fabrication

To prepare an evenly dispersed slurry, the as-synthesized carbon material, carbon black, and PTFE were uniformly mixed in ethanol with a mass ratio of 8:1:1. The slurry was dried at 80 °C for 12 h and then cut into 10 × 10 mm carbon films with a mass loading of approximately 3–5 mg cm^{-2}. A carbon film was pressed onto stainless-steel mesh current collectors or nickel foam under the pressure of 10 MPa for 1 min to fabricate an electrode. The electrochemical performance was evaluated using a three-electrode system, with KOH as the electrolyte, a Hg/HgO electrode as the reference electrode, and a platinum foil as the counter electrode. The ZIHCs were assembled using polished Zn foil with a thickness of 100 μm and a diameter of 16 mm as the anode and glass fiber as the separator. The CR2032 coin cell was constructed with 2 M $ZnSO_4$ aqueous solution as electrolyte to assess the characteristics of NHPCs in ZIHCs.

Electrochemical measurement

Cyclic voltammetry (CV) curves, galvanostatic charge/discharge (GCD) tests and electrochemical impedance spectroscopy (EIS) analysis were performed using a CHI 660E electrochemical workstation. The detailed information of CV, GCD, and EIS measurements was adopted from our previous reports[41]. The electrochemical measurements were conducted within a potential window of 0.2 to 1.8 V for the ZIHC device and −1.0 to 0 V for the three-electrode system.

The specific capacitance (C, F g^{-1}) was calculated by the discharge curves of GCD using the following equation (Eq. [1]):

$$C = \frac{I\Delta t}{m\Delta V} \tag{1}$$

The energy density (E, Wh kg^{-1}) and power density (P, W kg^{-1}) were evaluated by Eqs (2) and (3).

$$E = \frac{C\Delta V^2}{2 \times 3.6} \tag{2}$$

$$P = \frac{E \times 3,600}{\Delta t} \tag{3}$$

Results and discussion

Effect of activator to carbon precursor ratio on electrochemical performance

A model compound (lignin) was used as a biomass source to synthesize NHPCs through an integrated carbonization-activation process. The precursor mixture of PU and lignin (mass ratio 1:1) was combined with the activator at different mass ratios (3:1, 4:1, and 5:1) to optimize the resulting electrochemical performance. The electrochemical performance of the NHPCs, namely N-1@AC-3, N-1@AC-4, and N-1@AC-5, was initially evaluated using a typical three-electrode system in 6 M KOH electrolyte. The CV test in this study was conducted at scan rates ranging from 1 to 100 mV s^{-1} within a potential window of −1.0–0 V. At a scan rate of 50 mV s^{-1}, all carbonaceous materials exhibited quasi-rectangular CV curves (Fig. 1a), indicating a storage mechanism dominated by EDLC. Among them, N-1@AC-4 showed the larger CV curve area, indicating the higher specific capacitance. This finding was consistent with the constant GCD test results, which exhibited the longer discharge time of N-1@AC-4 at a current density of 1 A g^{-1} (Fig. 1b).

The specific capacitance of N-1@AC-3, N-1@AC-4, and N-1@AC-5 was calculated to be 206.6, 249.3, and 211.3 F g^{-1}, respectively (Fig. 1c). The rate capacitance (Fig. 1c) was evaluated at different current densities (0.1–20 A g^{-1}). Specifically, the specific capacitance initially increased and subsequently decreased as the amount of KOH increased. This nonlinear performance stemmed from the dual effects of KOH activation. A moderate degree of activation (N-1@AC-4) etched the carbon skeleton to generate rich micropore-mesoporous structures (with a specific surface area of

https://doi.org/10.48130/scm-0026-0010

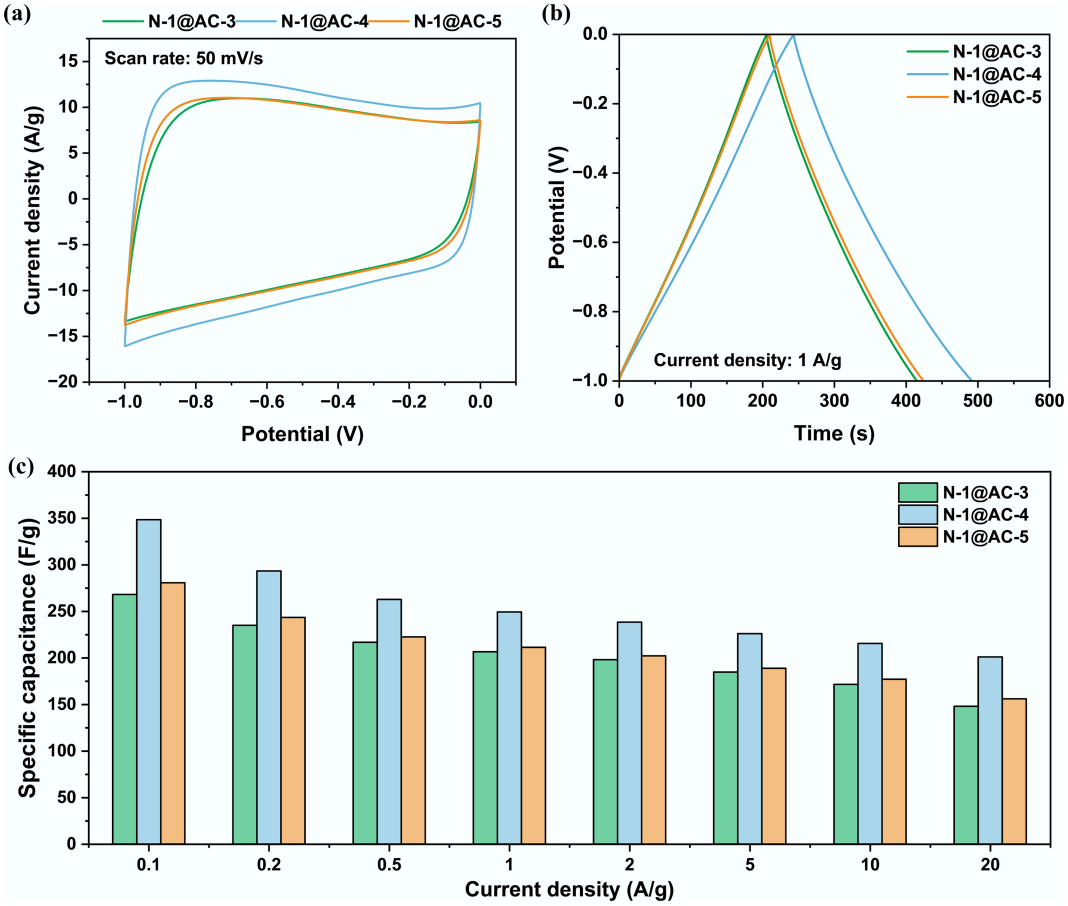

Fig. 1 Effect of activator to carbon precursor ratio on electrochemical performance in a three-electrode system: (**a**) Cyclic voltammogram curves at a scan rate of 50 mV s^{-1}; (**b**) Galvanostatic charge and discharge curves at a current density of 1 A g^{-1}; and (**c**) Specific capacitance at different current densities.

1,270.9 m^2 g^{-1}), thereby providing more active sites for ion adsorption. However, excessive activation with KOH (N-1@AC-5) caused the collapse of pore walls and a reduction in mesoporous volume, consequently reducing the specific surface area and damaging the conductive network, which ultimately compromised the rate performance. Accordingly, an optimal carbon precursor to activator mass ratio of 1:4 contributed to the preparation of porous carbonaceous materials with superior electrochemical performance.

To systematically study the electrochemical performance of NHPCs, they were assembled into typical ZIHCs using 2 M $ZnSO_4$ aqueous electrolyte. The CV curves measured at a scan rate of 50 mV s^{-1} (Fig. 2a) exhibited a typical quasi-rectangular shape. The presence of distinct redox peaks superimposed on these curves suggests the occurrence of Faradaic reactions. This observation further confirmed a synergic energy storage mechanism involving both the double-layer capacitance and pseudo-capacitance. It was notable that the N-1@AC-4 exhibited a larger CV area, indicating a higher specific capacity of 302.5 F g^{-1} at a current density of 0.1 A g^{-1}. This result was consistent with the findings from the three-electrode measurements, confirming the consistency between the intrinsic properties of the material and the structure-activity relationship of the device. GCD measurements were performed to characterize the energy storage properties of ZIHCs. At a current density of 1 A g^{-1}, the GCD curve of the N-1@AC-4 exhibited a highly symmetrical triangular profile, demonstrating excellent electrochemical reversibility, which was attributed to its well-developed hierarchical pore structure (Fig. 2b). As the current density increased, the N-1@AC-3 and N-1@AC-5 exhibited a more pronounced capacity fading and the capacity was significantly lower than N-1@AC-4 (Fig. 2c). The disparity in rate performance primarily originated from the distinct pore structures resulting from different activation degrees. For N-1@AC-3, insufficient KOH activation led to a relatively low specific surface area, thereby limiting the rapid transport of ions. Conversely, the excessive activation in N-1@AC-5 induced the collapse of pore walls, which compromised the rapid ion transport and impaired the conductive network.

Influence of N-promoter incorporation on electrochemical performance

Characterization of varying N proportion in NHPCs

To investigate the electrochemical performance of NHPCs, a series of characterizations were conducted. SEM images (Fig. 3a and Supplementary Fig. S1) confirmed that the NHPCs possessed hierarchical porous structures. Specifically, the carbonization of PU typically generated a macroporous framework via gas evolution, while the subsequent KOH activation created micro- and meso-pores via chemical etching. Overall, the KOH activation promoted the development of the porous structure, thereby shortening ion-diffusion distances and expanding the electrode–electrolyte contact area[41]. Elemental mapping of N-3@AC-4 (Fig. 3a) showed a highly uniform distribution of N and O species across the carbon matrix surface. The crystal structures of NHPCs were evaluated by XRD analysis (Supplementary Fig. S2). The patterns exhibited significantly broadened diffraction peaks at near

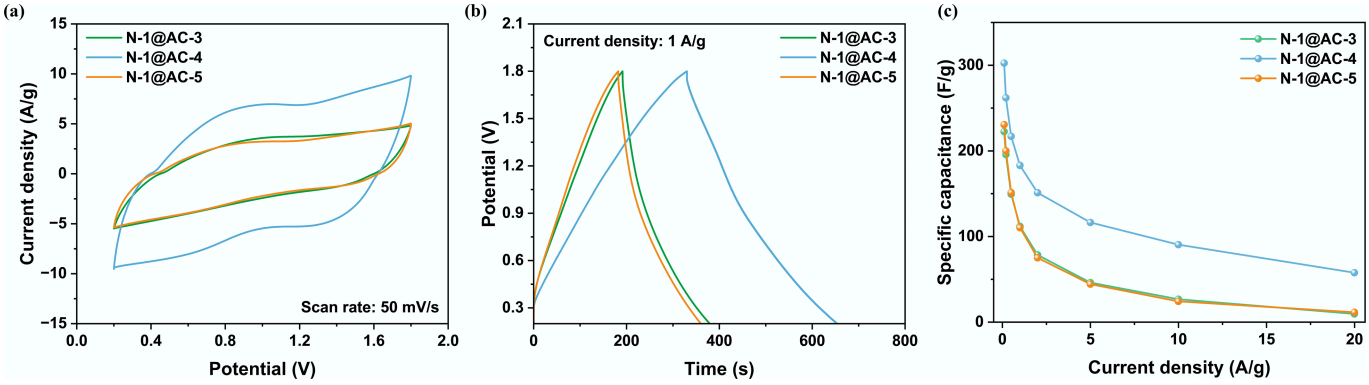

Fig. 2 Effect of activator to carbon precursor ratio on electrochemical performance in ZIHCs: (**a**) Cyclic voltammogram curves at a scan rate of 50 mV s^{-1}; (**b**) Galvanostatic charge and discharge curves at a current density of 1 A g^{-1}; and (**c**) Specific capacitance at different current densities.

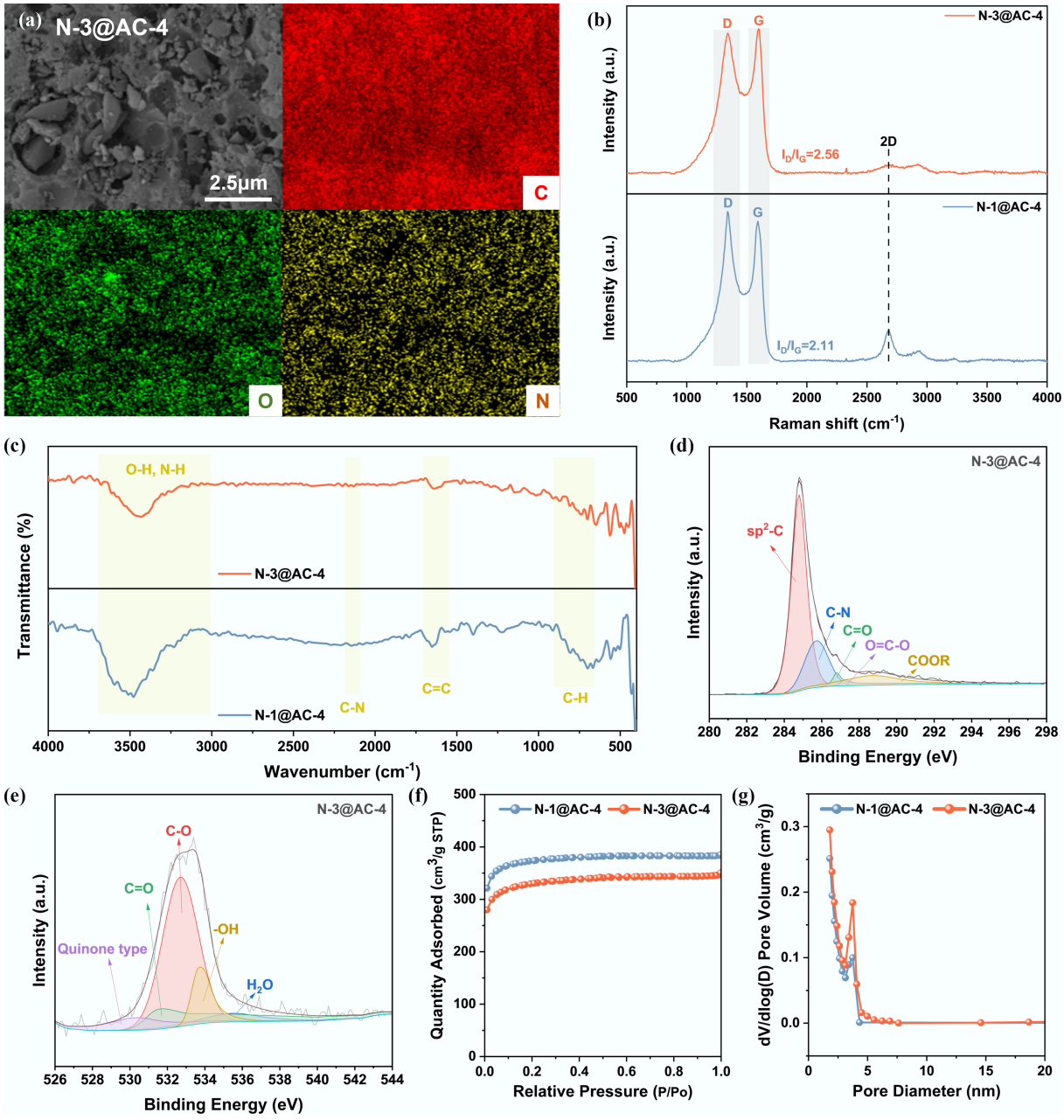

Fig. 3 Physicochemical characteristics of NHPCs: (**a**) SEM images and EDS elemental maps of N-3@AC-4; (**b**) Raman spectra; (**c**) FTIR spectra; (**d**), (**e**) High-resolution XPS C 1s and O 1s spectra of N-3@AC-4; (**f**) N_2 sorption-desorption isotherms; and (**g**) Pore size distribution.

https://doi.org/10.48130/scm-0026-0010

$2\theta \approx 22°$, corresponding to the (002) plane diffraction of amorphous carbon[42].

Raman spectra of the NHPCs (Fig. 3b) displayed distinct D and G bands associated with lattice defects and graphitic ordering, respectively. The higher I_D/I_G ratio of N-3@AC-4 (2.56) relative to N-1@AC-4 (2.11), suggested increased defect density and structural disorder with higher nitrogen content. Surface functional groups of NHPCs were verified by the FTIR analysis, as demonstrated in Fig. 3c. The retention of the inherent aromatic framework of lignin was evidenced by the characteristic C=C stretching vibration at 1,605 cm^{-1} and aliphatic C–H bending vibrations in the 900–650 cm^{-1} range[43,44]. The successful incorporation of N was manifested by two key indicators. The superposition of N–H stretching vibrations (from precursor decomposition) within the 3,700–3,000 cm^{-1} band and the emergence of C–N bonds at 2,171 and 2,117 cm^{-1}[45]. This synergistic modification preserves the intrinsic functional groups (e.g., hydroxyl and carbonyl) from lignin while simultaneously introducing active C–N sites.

XPS analysis (Supplementary Fig. S3) further confirmed the coexistence of C, N, and O elements in N-3@AC-4, with N and O contents of 1.72 at.% and 9.50 at.%, respectively. The high-resolution C 1s spectrum (Fig. 3d) displayed five chemical states: sp^2-C (284.6 eV, dominant), C–N (285.7 eV), C=O (286.3 eV), O=C–O (287.2 eV), and COOR (288.5 eV)[46]. The high-resolution O 1s spectrum (Fig. 3e) revealed five distinct peaks corresponding to quinone oxygen (530.4 eV), C=O (531.6 eV), C–O (532.8 eV), –OH (533.4 eV), and H_2O (535.5 eV)[47]. The N 1s spectrum (Supplementary Fig. S4) could be deconvoluted into four components assigned to pyridinic-N, pyrrolic-N, graphitic-N, and N-oxides[48]. It is well established that pyridinic-N and pyrrolic-N are crucial for superior capacitance, whereas graphitic-N contributes minimally to active sites for surface reactions[49]. Thus, this strategy offers a dual advantage in the design of high-performance energy storage materials. The aromatic skeleton ensured high electronic conductivity, while the nitrogen-doped sites enhanced the electrochemical activity and electronic conductivity[50].

The N_2 adsorption-desorption isotherms (Fig. 3f) revealed that the representative NHPCs exhibited typical Type I adsorption isotherm characteristics. The sharp increase in adsorption capacity observed at the low-pressure region ($P/P_0 < 0.5$) was attributed to the presence of abundant microporous structures within the materials. The pore size distribution curves of the NHPCs (Fig. 3g) revealed a hierarchical porous structure, with the predominant distribution peaks located in the 2–4 nm range. The synergistic effect of the hierarchical porous structure significantly enhances the electrochemical performance of NHPCs, where micropores provide abundant Zn^{2+} adsorption sites[51], while mesopores and macropores serve as ion transport channels and electrolyte reservoirs[11], thereby collectively facilitating rapid ion transportation and storage. The NHPCs exhibited high BET specific surface area exceeding 1,100 $m^2\ g^{-1}$ (Table 1), highlighting their potential as cathode materials. However, an inverse correlation was observed between the nitrogen loading and the specific surface area. This phenomenon was attributed to the partial collapse of the porous framework, initially formed from the PU precursor during primary carbonization, which underwent etching in the subsequent KOH activation step.

Electrochemical evaluation

As the ratio of activator to carbon precursor was optimized at 4:1, the NHPCs were examined in both a typical three-electrode system and ZIHCs as a function of the mass ratio of PU to lignin. In the three-electrode system, the CV curves measured at a scan rate of 50 mV s^{-1} (Fig. 4a) exhibited a quasi-rectangular shape, indicating the characteristic electrical double-layer capacitance behavior. The larger CV curve area of N-3@AC-4 was observed, confirming its superior specific capacitance. The CV curves of N-3@AC-4 measured at different scan rates (Fig. 4b) exhibited no significant distortion, demonstrating its excellent rate capability. The GCD curves at a current density of 1 A g^{-1} are shown in Fig. 4c. With the increased usage of PU, the specific capacitance was significantly enhanced, increasing from 249.3 F g^{-1} (N-1@AC-4) to 269.1 F g^{-1} (N-3@AC-4). The performance enhancement was due to the synergistic effect of N-doping and hierarchically porous structures: suitable N-species (pyridinic-/pyrrolic-N) impart improved wettability and conductivity, while the nitrogen-containing gases from PU carbonization enabled a mesoporous architecture conducive to ion transport, aligning with BET findings.

In contrast, a further increase in the mass ratio of PU to lignin (4:1) resulted in a decline in specific capacitance to 267.8 F g^{-1}. It might be attributed to the formation of electrochemically inert graphitic nitrogen due to excessive doping, which increased the defect density in the sp^2-carbon network and blocked intrinsic active sites, ultimately leading to diminished conductivity[41]. As the scan rate increased, the GCD curves of N-3@AC-4 maintained excellent symmetry (Fig. 4d), indicating superior rate capacitance. At the current densities of 0.1, 0.2, 0.5, 1, 2, 5, 10, and 20 A g^{-1}, the average discharge capacities of N-3@AC-4 in the three-electrode system were 430.6, 338.6, 287.3, 269.1, 256.2, 242.8, 233.5, and 222.0 F g^{-1}, respectively (Fig. 4e).

To investigate the energy behavior, EIS analysis was conducted in a three-electrode system. The Nyquist plots (Fig. 4f) showed that all NHPCs exhibited semi-circles in the high-frequency region, which was attributed to the interfacial charge transfer in parallel with the double-layer capacitance. The diagonal line in the low-frequency region corresponded to the ion diffusion. It is worth noting that N-3@AC-4 exhibited the outstanding kinetic characteristics: the slope of its low-frequency region slash was close to 90° (Fig. 4f), significantly steeper than N-1@AC-4, suggesting more efficient double-layer charging and enhanced ion diffusion rates. Meanwhile, the Nyquist plot of N-3@AC-4 exhibited a smaller high-frequency semicircular diameter, indicating low charge transfer resistance (R_{ct}), which was attributed to its optimized pore structure and favorable heteroatom content. The higher resistance of N-1@AC-4 could be attributed to the higher proportion of oxygen-containing functional groups (e.g., C-O, O-H, -COOH), which impede electron conduction and increase the resistance of materials[52,53].

To further evaluate the energy storage characteristics, the current contributions from capacitive- and diffusion-controlled processes

Table 1 Textural characteristics of NHPCs

Materials	S_{BET}[a] ($m^2\ g^{-1}$)	S_{mic}[b] ($m^2\ g^{-1}$)	S_{mes}[c] ($m^2\ g^{-1}$)	V_{total}[d] ($cm^3\ g^{-1}$)	V_{mic}[b] ($cm^3\ g^{-1}$)	V_{mes}[c] ($cm^3\ g^{-1}$)	D_{avg}[e] (nm)
N-1@AC-4	1,271	1,108	163	0.596	0.505	0.091	1.88
N-3@AC-4	1,133	935	198	0.542	0.423	0.119	1.91

[a] S_{BET} is BET specific surface area; [b] S_{mic} is microporous surface area and V_{mic} is microporous pore volume are calculated by *t*-plot method; [c] S_{mes} is mesoporous surface area determined by the t-plot method external surface area ($S_{mes} = S_{BET} - S_{mic}$) and V_{mes} is mesoporous pore volume ($V_{mes} = V_{total} - V_{mic}$); [d] V_{total} is total volume acquired at $P/P_0 = 0.99$; [e] D_{avg} is average pore diameter calculated by $4V_{total}/S_{BET}$.

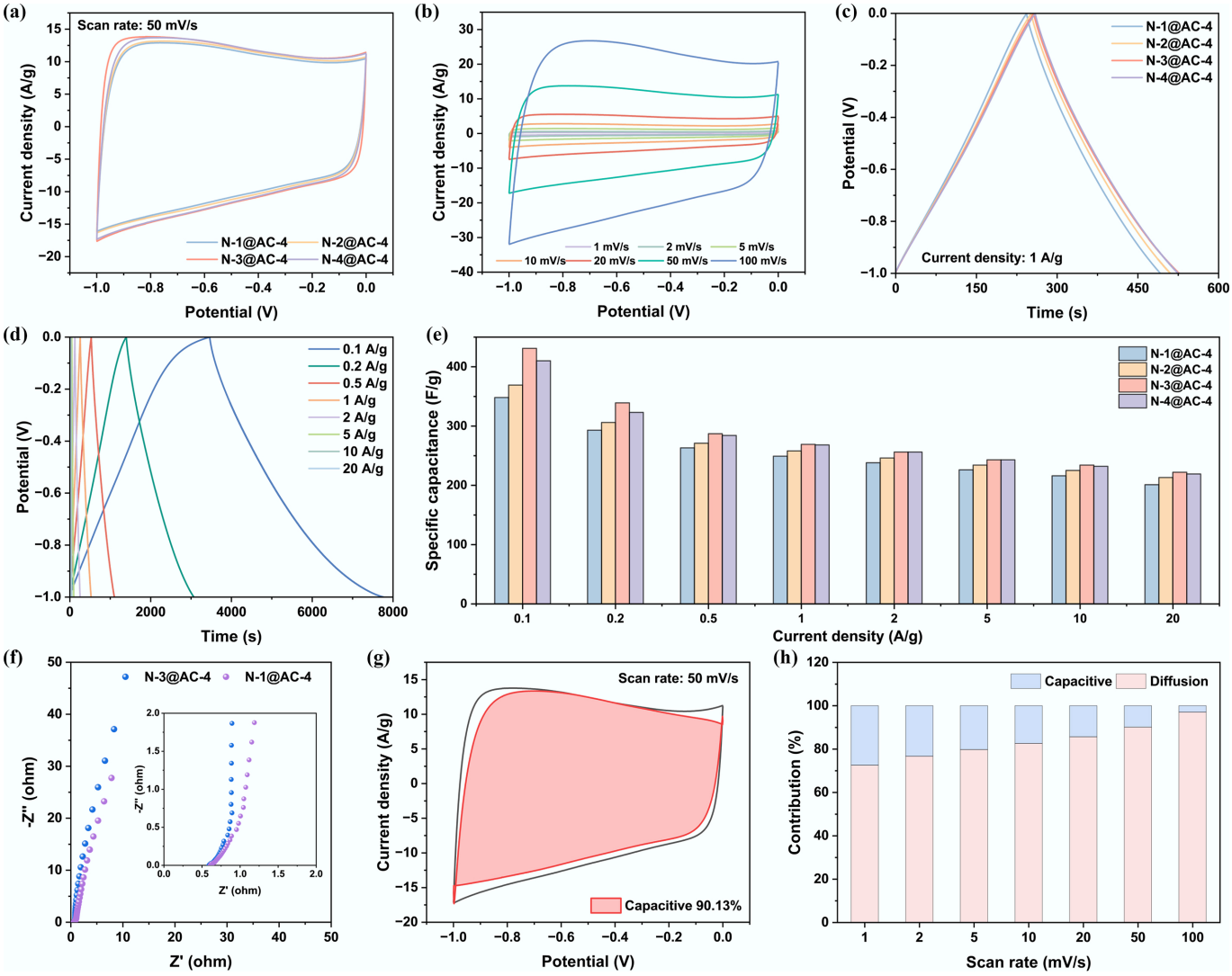

Fig. 4 Influence of PU to lignin ratio on electrochemical performance in a three-electrode system: (**a**) Cyclic voltammogram curves at a scan rate of 50 mV s^{-1}; (**b**) Cyclic voltammogram curves of N-3@AC-4 at different scan rates; (**c**) Galvanostatic charge and discharge curves at a current density of 1 A g^{-1}; (**d**) Galvanostatic charge and discharge curves of N-3@AC-4 at different current densities; (**e**) Specific capacitance at different current densities; (**f**) Nyquist plots of N-1@AC-4 and N-3@AC-4; (**g**) Capacitive contribution of N-3@AC-4 at 10 mV s^{-1}; and (**h**) Diffusion-capacitive contribution ratio of N-3@AC-4.

were quantified by analyzing the CV data (Eqs [4] and [5]), in which the terms k_1v and $k_2v^{1/2}$ correspond to the fast kinetic (capacitive-controlled) and slow dynamic (diffusion-controlled) processes, respectively. As shown in Fig. 4g, at a scan rate of 50 mV s^{-1}, the capacitance contribution of N-3@AC-4 exceeded 90%, demonstrating the dominance of surface-controlled process in the energy storage mechanism. The capacitance contribution exceeded 97% at a high scan rate of 100 mV s^{-1}, indicating its dominance in the charge storage mechanism and the excellent rate capacitance performance of N-3@AC-4 (Fig. 4h). The outstanding electrochemical performance of N-3@AC-4 in a typical three-electrode system was attributed to its high BET specific surface area, favorable pore size distribution, and appropriate amounts of heteroatoms in the carbon matrix. Therefore, the cathode materials with outstanding electrochemical performance in a 6 M KOH electrolyte were successfully prepared by systematically optimizing the key synthesis parameters, with an activator to precursor ratio of 4:1 and a PU to lignin ratio of 3:1.

$$i = k_1v + k_2v^{1/2} \quad (4)$$

$$i/v^{1/2} = k_1v^{1/2} + k_2 \quad (5)$$

As for NHPCs tested in the ZIHCs, the CV profiles measured at 50 mV s^{-1} (Fig. 5a) were quasi-rectangular while exhibiting asymmetric current responses, suggesting a synergistic effect between double-layer capacitance and faradaic pseudo-capacitance. Furthermore, the CV curves remained free of characteristic peaks for water decomposition (i.e., oxygen or hydrogen evolution) within the potential window range of 0.2–1.8 V (Fig. 5a), confirming its ideal operational stability within this wide electrochemical range[41]. The presence of clear redox peaks across all CV profiles indicated the occurrence of Faraday reactions, attributed to the nitrogen-containing functional groups on the material surface during charging and discharging. These N-doped species served as additional active centers, which significantly enhanced the electronic conductivity and ion adsorption capacity of the carbon matrix, thereby contributing to the outstanding rate performance.

https://doi.org/10.48130/scm-0026-0010

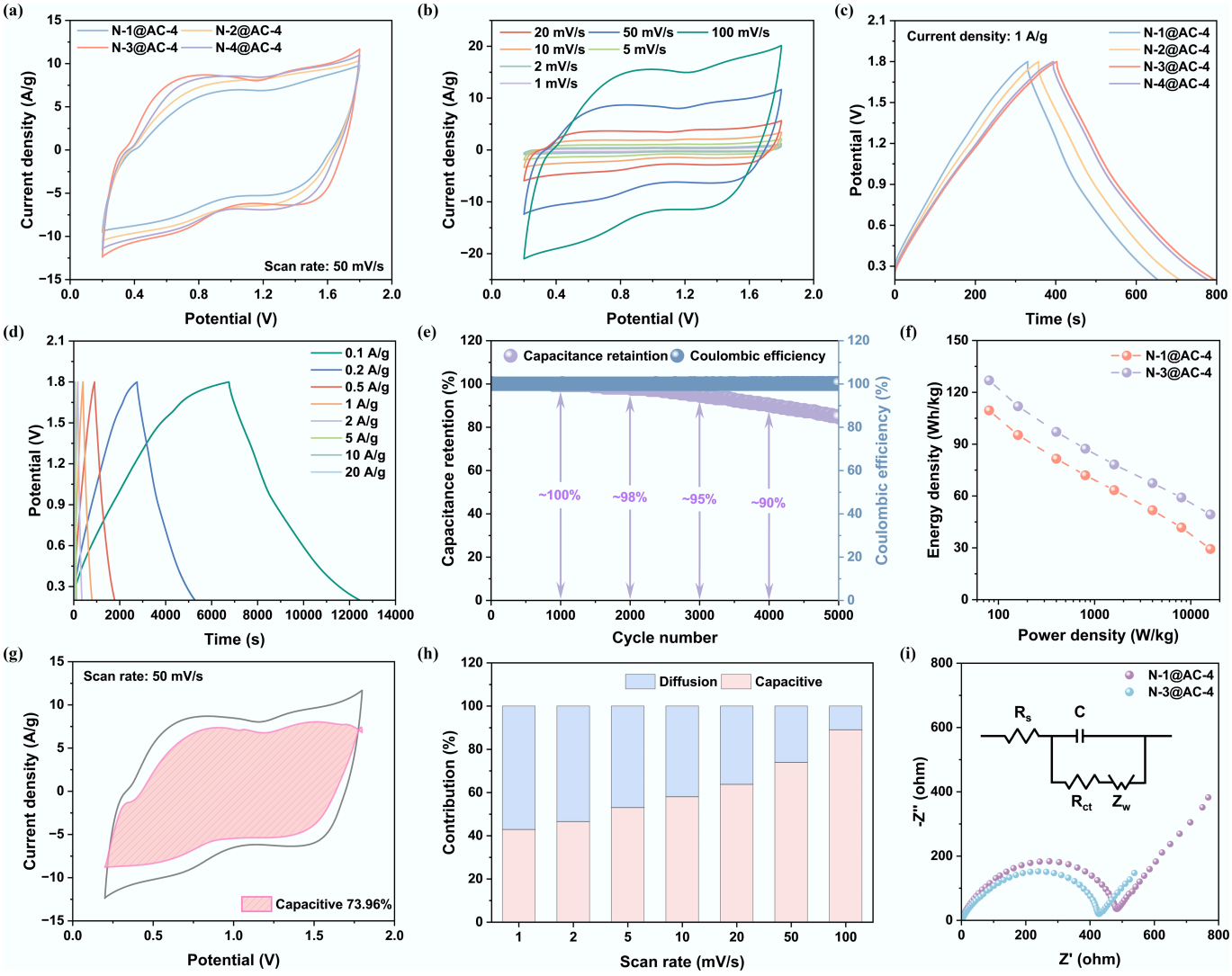

Fig. 5 Influence of PU to lignin ratio on electrochemical performance in ZIHCs: (**a**) Cyclic voltammogram curves at a scan rate of 50 mV s^{-1}; (**b**) Cyclic voltammogram curves of N-3@AC-4 at different scan rates; (**c**) Galvanostatic charge and discharge curves at a current density of 1 A g^{-1}; (**d**) Galvanostatic charge and discharge curves of N-3@AC-4 at different current densities; (**e**) Cycling performance of N-3@AC-4; (**f**) Energy-power density; (**g**) Capacitive contribution at 50 mV s^{-1}; (**h**) Diffusion-capacitive contribution ratio of N-3@AC-4; and (**i**) Nyquist plots of N-1@AC and N-3@AC-4.

To analyze the dynamic reaction of N-3@AC-4, CV measurements at different scan rates were further performed (Fig. 5b). At low scan rates, the CV curve exhibited a quasi-rectangular shape, indicating that the charge storage was dominated by the EDLC mechanism. When the scan rate was increased to 100 mV s^{-1}, the emergence of distinct redox peaks confirmed the additional contribution of faradaic pseudo-capacitance to the overall energy storage. This pseudo-capacitive behavior originated from the nitrogen- and oxygen-containing functional groups incorporated into the carbon skeleton. These functional groups introduced additional faradaic capacitance by undergoing reversible redox reactions with Zn^{2+} ions[54]. At high scan rates, the well-preserved shape of the CV curves confirmed the exceptional charge transport kinetics of the N-3@AC-4 electrode. This outstanding performance was a direct consequence of its hierarchical porous architecture and optimal nitrogen doping level, which synergistically enhanced ion diffusion and electron conduction.

The GCD curves (Fig. 5c) exhibited highly symmetrical triangular characteristics, confirming rapid charge-transfer kinetics and exceptional electrochemical reversibility, consistent with ideal capacitive energy storage behavior. The enhancement in specific capacitance from nitrogen doping was clearly demonstrated by the superior performance of the N-3@AC-4 compared to the N-1@AC-4 with lower nitrogen content. This improved performance was attributed to the formation of C–N bonds via N-doping in the carbon matrix, which contributed to an increase in negative charge density and a reduction in the Zn^{2+} adsorption energy barrier, collectively enabling enhanced charge storage. The excellent rate performance of N-3@AC-4, as evidenced by its GCD curves from 0.1 to 20 A g^{-1} (Fig. 5d), coupled with the high specific capacitance (356.9 F g^{-1}) at 0.1 A g^{-1} (Table 2), underscored the beneficial role of nitrogen doping in improving the electrochemical properties of electrode materials. Notably, the N-3@AC-4 exhibited a superior specific capacitance compared to representative N-doped carbon materials documented in the literature (Table 3).

The long-term cycling stability of the N-3@AC-4 was evaluated over 5,000 charge-discharge cycles at a current density of 5 A g^{-1} in

Table 2 Specific capacitance (F g^{-1}) of NHPCs in ZIHCs

Sample	Current density (A g^{-1})							
	0.1	0.2	0.5	1	2	5	10	20
N-1@AC-4	302.5	262.0	216.9	182.9	151.1	116.3	90.3	57.5
N-2@AC-4	320.3	287.5	247.3	218.1	192.9	167.2	142.8	110.6
N-3@AC-4	356.9	314.8	273.1	245.6	220.0	189.7	166.3	138.8
N-4@AC-4	351.9	310.6	267.7	239.4	214.2	183.6	159.7	129.4

Table 3 Comparison of capacitive performance between the representative studies and this work

Material	Feedstock	Nitrogen precursor	Specific capacitance	Energy density	Ref.
NSLHPC	Enzymatic hydrolysis lignin	Potassium thiocyanide	295 F g^{-1}@0.2 A g^{-1}	104.9 Wh kg^{-1}@160.6 W kg^{-1}	[55]
L-NS-CNS	Sodium lignosulfonate	NH_4Cl and thiourea	233.4 F g^{-1}@0.1 A g^{-1}	33.8 Wh kg^{-1}@9.9 W kg^{-1}	[56]
NLPC1000	Enzymatic hydrolysis lignin	NH_3	179 F g^{-1}@0.1 A g^{-1}	72.8 Wh kg^{-1}@86.4 W kg^{-1}	[57]
LNPC800	Sodium lignosulfonate	Melamine	266 F g^{-1}@0.05 A g^{-1}	–	[58]
NOPC-KOH-700	Alkali lignin	Melamine	311 F g^{-1}@0.1 A g^{-1}	111 Wh kg^{-1}@52 W kg^{-1}	[28]
NPC-5	Cationic polyacrylamide	–	115.44 mAh g^{-1}@0.1 A g^{-1}	85.3 Wh kg^{-1}@106.67 W kg^{-1}	[59]
CP-HPC	Chitosan-PET	–	354.2 F g^{-1}@0.5 A g^{-1}	120.36 Wh kg^{-1}@389 W kg^{-1}	[49]
N-3@AC-4	Dealkalized lignin	Polyurethane	356.9 F g^{-1}@0.1 A g^{-1}	126.89 Wh kg^{-1}@80 W kg^{-1}	This work

the ZIHCs system. Remarkably, the N-3@AC-4 exhibited exceptional stability, demonstrating ~100% capacitance retention over the 1,000 cycles, and maintaining a high retention rate of approximately 85% with a coulombic efficiency close to 100% after 5,000 cycles (Fig. 5e). The slight capacity decay was attributed to the loss of pore connectivity and the formation of Zn dendrites from accumulated reaction byproducts during cycling, which collectively exacerbated ion transport barriers and reduced the accessibility of active sites[49]. The Ragone plots (Fig. 5f) exhibited that N-3@AC-4 delivered a superior energy density of 126.89 Wh kg^{-1} at a power density of 80 W kg^{-1}. Notably, at higher power density (16,000 W kg^{-1}), it maintained a substantial energy density of 49.33 Wh kg^{-1}, demonstrating its exceptional comprehensive performance.

The capacitive contribution of N-3@AC-4 surged from 42% to 89% of the total current as the scan rate increased from 1 to 100 mV s^{-1} (Fig. 5g, h), which was attributed to the surface-controlled charge storage process[60]. The hierarchical pore architecture of N-3@AC-4 provided an ideal platform for rapid surface processes by offering abundant active sites and short ion diffusion paths, ensuring the dominance of the capacitive mechanism at high scan rates and resulting in outstanding rate capability. Further insights into the ion transport kinetics were analyzed from the Nyquist plot (Fig. 5i). The N-3@AC-4 demonstrated superior kinetics, as evidenced by a smaller semicircle in the medium-frequency region, suggesting reduced charge transfer resistance and a steep low-frequency line indicating low Warburg impedance. Overall, the electrochemical characterization showed that ZIHCs incorporating NHPCs exhibited excellent performance, demonstrating a successful combination of high energy density with high power density. Post-cycling physicochemical characterization of electrodes to study side reactions is challenging due to cell disassembly risks and additive interference; thus, *in situ*/operando techniques are essential for tracking material evolution during cycling.

Optimization of carbon precursor source upon electrochemical performance

Based on the established preparation conditions, this study systematically evaluated the feasibility of utilizing several representative biomass sources as precursors for high-performance electrode materials. The NHPCs synthesized from reed, corn stover, pine sawdust, and lignin under the optimized synthetic conditions were defined as N-3@AC-RD, N-3@AC-CS, N-3@AC-PS, and N-3@AC-DL, respectively. In the three-electrode system, the CV curves (Fig. 6a) showed a typical rectangular shape within the −1.0–0 V potential window, indicating that the charge storage mechanism was dominated by double-layer capacitors. The GCD curves (Fig. 6b) measured at a current density of 1 A g^{-1} presented a symmetrical isosceles triangle shape, indicating highly reversible capacitive behavior. The specific capacitances of the N-3@AC-RD and N-3@AC-PS were comparable to the N-3@AC-DL (Fig. 6c). Overall, biomass-derived carbonaceous materials showed promising commercial application prospects, attributed to their low cost combined with competitive electrochemical performance.

The electrochemical performance of the four electrode materials was also systematically examined in ZIHCs (Fig. 7). The results indicated that N-3@AC-DL exhibited the best performance, while the other three materials demonstrated relatively inferior properties. The performance disparity can be attributed to several factors: Zn^{2+} diffusion was hindered by the restrictive pore structure inherent to the biomass precursors, which significantly compromised ion transport kinetics at elevated current densities; the intrinsic nitrogen content in biomass promoted the formation of excessive N species within the carbon matrix, which occupied the active sites, thereby degrading the bulk electrical conductivity and diminishing the specific capacitance[61]; the presence of oxygen-containing functional groups on the biochar surface triggered irreversible side reactions, resulting in a marked rise in interfacial impedance[53].

The long-term cycling stability of N-3@AC-PS, N-3@AC-CS, and N-3@AC-RD in ZIHCs was evaluated at a current density of 5 A g^{-1} (Fig. 7d–f). Notably, the capacitance retention gradually increased after an initial drop, which can be attributed to electrode activation associated with the more complex pore structures of biomass-derived carbon materials[49]. After 5,000 cycles, N-3@AC-PS and N-3@AC-CS exhibited comparable capacitance retention rates of 93.5% and 93.2%, respectively, while maintaining ~100% coulombic efficiency. In contrast, the cycling test of N-3@AC-RD was terminated after 4,500 cycles due to a sharp decline in capacitance retention. The intricate porous architecture of N-3@AC-RD led to elongated ion transport pathways and internal pore clogging, which impeded ion diffusion, increased resistance, and ultimately caused capacity decay[49]. Accordingly, these findings underscore the necessity for further optimization of biomass-derived materials for application in ZIHCs.

https://doi.org/10.48130/scm-0026-0010

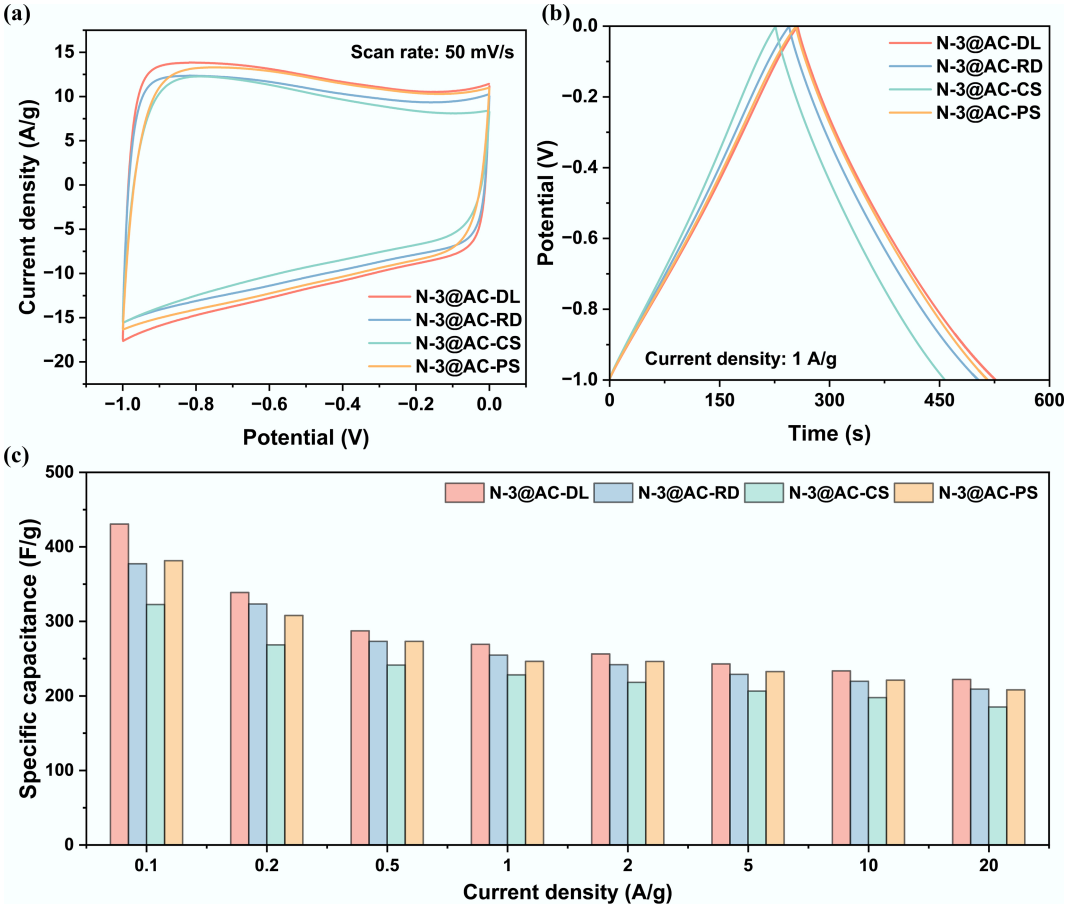

Fig. 6 Optimization of carbon precursor source of NHPCs in a three-electrode system: (**a**) Cyclic voltammogram curves at a scan rate of 50 mV s^{-1}; (**b**) Galvanostatic charge and discharge curves at a current density of 1 A g^{-1}; and (**c**) Specific capacitance at different current densities.

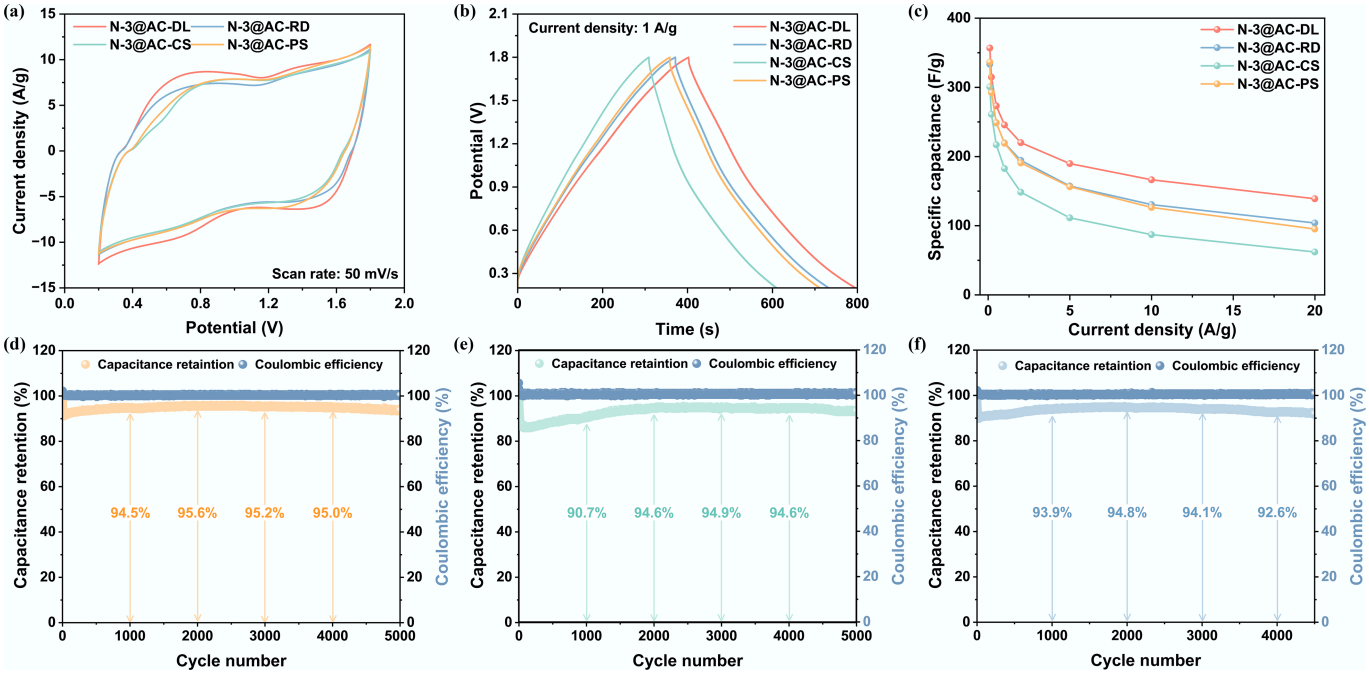

Fig. 7 Optimization of carbon precursor source of NHPCs in ZIHCs: (**a**) Cyclic voltammogram curves at a scan rate of 50 mV s^{-1}; (**b**) Galvanostatic charge and discharge curves at a current density of 1 A g^{-1}; (**c**) Specific capacitance at different current densities; and (**d**)–(**f**) Cyclic stability of N-3@AC-PS, N-3@AC-CS, and N-3@AC-RD.

Conclusions

In summary, this study developed a sustainable route to synthesize high-performance carbonaceous cathode materials for ZIHCs through co-carbonization of biomass and nitrogen-rich plastic waste (PU), followed by KOH activation. The obtained N-3@AC-4 exhibited outstanding electrochemical properties: a high specific capacitance of 430.6 F g^{-1} even at 0.1 A g^{-1} in a three-electrode system, which remains at 356.9 F g^{-1} in ZIHCs, along with a superior energy density of 126.89 Wh kg^{-1} at 80 W kg^{-1} and long-term stability with ~85% capacitance retention after 5,000 cycles at 5 A g^{-1}. This study establishes a scalable production strategy for high-performance aqueous ZIHCs cathodes derived from waste resources and highlights their promise for grid-scale energy storage. Future efforts should prioritize tailoring pore architecture and heteroatom doping for further enhancing energy density in practical devices.

Supplementary information

It accompanies this paper at: https://doi.org/10.48130/scm-0026-0010.

Author contributions

The authors confirm contributions to the paper as follows: Conceptualization: Guanyu Zhang; methodology: Guanyu Zhang; software: Guanyu Zhang; formal analysis: Guanyu Zhang; investigation: Guanyu Zhang, Tianqi Cao, Zengjian Guo; supervision: Xuesong Zhang, Lujia Han; writing – original draft: Guanyu Zhang; writing – review and editing: Xuesong Zhang; project administration: Xuesong Zhang, Lujia Han; funding acquisition: Xuesong Zhang, Lujia Han. All authors reviewed the results and approved the final version of the manuscript.

Data availability

The datasets used or analyzed during the current study are available from the corresponding author on reasonable requests.

Funding

This work was supported by National Natural Science Foundation of China (52206290), the Disciplinary Breakthrough Project of Ministry of Education (MOE, #00975101), and the earmarked fund for CARS (Grant No. 36).

Declarations

Competing interests

The authors declare that they have no known competing financial interests or personal relationships that could have appeared to influence the work reported in this paper.

Author details

Engineering Laboratory for AgroBiomass Recycling & Valorizing, College of Engineering, China Agricultural University, Beijing 100083, China

References

[1] Zhang Z, Chen Y, Ma T, Tian H, Liu J, et al. 2025. Multi-type energy storage expansion planning: a review for high-penetration renewable energy integration. *Renewable and Sustainable Energy Reviews* 219:115853

[2] Zhang Y, Fan L, Liu S, Zhou N, Ding K, et al. 2018. Microwave-assisted co-pyrolysis of brown coal and corn stover for oil production. *Bioresource Technology* 259:461–464

[3] Shen B, Hove A, Hu J, Dupuy M, Bregnbæk L, et al. 2024. Coping with power crises under decarbonization: the case of China. *Renewable and Sustainable Energy Reviews* 193:114294

[4] Mirkin CA, Sargent EH, Schrag DP. 2024. Energy transition needs new materials. *Science* 384:713

[5] Zhang X, Cao T, Zhang G, Liu Q, Kong G, et al. 2024. Sustainable hydrothermal carbon for advanced electrochemical energy storage. *Journal of Materials Chemistry A* 12:4996–5039

[6] Liao Q, Wan S, Liu Y, Niu X, Zhang D, et al. 2025. Hemp-derived hierarchically porous carbon cathode enabling high energy storage for advanced zinc-ion hybrid capacitor. *Journal of Energy Storage* 115:115975

[7] Wei F, Zeng Y, Guo Y, Li J, Zhu S, et al. 2023. Recent progress on the heteroatom-doped carbon cathode for zinc ion hybrid capacitors. *Chemical Engineering Journal* 468:143576

[8] Liang Y, Yao Y. 2023. Designing modern aqueous batteries. *Nature Reviews Materials* 8:109–122

[9] Li J, Ge K, Grammenos AO, Taberna PL, Simon P, et al. 2025. Understanding multi-stage charge storage on nanoporous carbons in Zn-ion hybrid capacitors. *Advanced Materials* 37:2502422

[10] Yang G, Zhang Q, He C, Gong Z, Liu Z, et al. 2025. Bionic hollow porous carbon nanofibers for energy-dense and rapid zinc ion storage. *Angewandte Chemie International Edition* 64:e202421230

[11] Hou Y, Li X, Zhang X, Sun M, Li M, et al. 2024. Pyrrolic-N-B bonds mediated local charge distribution for boosting the capacitance of aqueous zinc-ion hybrid supercapacitors. *Materials Today Sustainability* 26:100785

[12] Sun R, Xia P, Guo X, Dong S, Xu F, et al. 2024. Ternary $Zn_3V_3O_8$ superstructure and synergistic modification of separator promote high performance and stable zinc ion battery. *Chemical Engineering Journal* 486:150377

[13] Hao J, Zhang S, Wu H, Yuan L, Davey K, et al. 2024. Advanced cathodes for aqueous Zn batteries beyond Zn^{2+} intercalation. *Chemical Society Reviews* 53:4312–4332

[14] Jin J, Geng X, Chen Q, Ren TL. 2022. A better Zn-ion storage device: recent progress for Zn-ion hybrid supercapacitors. *Nano-Micro Letters* 14:64

[15] Lu Y, Li Z, Bai Z, Mi H, Ji C, et al. 2019. High energy-power Zn-ion hybrid supercapacitors enabled by layered B/N co-doped carbon cathode. *Nano Energy* 66:104132

[16] Xu Z, Sun Z, Shan J, Jin S, Cui J, et al. 2024. O, N-codoped, self-activated, holey carbon sheets for low-cost and high-loading zinc-ion supercapacitors. *Advanced Functional Materials* 34:2302818

[17] Wang H, Chen X, Zhang J, Yuan Z, Ye P, et al. 2022. Unveiling the cooperative roles of pyrrolic-N and carboxyl groups in biomass-derived hierarchical porous carbon nanosheets for high energy-power Zn-ion hybrid supercapacitors. *Applied Surface Science* 598:153819

[18] Liu X, Tong Y, Wu Y, Zheng J, Sun Y, et al. 2022. Synergistically enhanced electrochemical performance using nitrogen, phosphorus and sulfur tri-doped hollow carbon for advanced potassium ion storage device. *Chemical Engineering Journal* 431:133986

[19] Tong Y, Wu Y, Liu Z, Yin Y, Sun Y, et al. 2023. Fabricating multi-porous carbon anode with remarkable initial coulombic efficiency and enhanced rate capability for sodium-ion batteries. *Chinese Chemical Letters* 34:107443

[20] Liu X, Yu X, Tong Y, Sun Y, Mai W, et al. 2022. Potassium storage in bismuth nanoparticles embedded in N-doped porous carbon facilitated by ether-based electrolyte. *Chemical Engineering Journal* 446:137329

[21] Qiu T, Xie K, Liu C, Ahmad F, Zhao W, et al. 2025. Microwave-assisted pyrolysis for advanced sustainable carbon materials. *Sustainable Carbon Materials* 1:e011

[22] Cai S, Zhou X, Wang Y, Lu X. 2025. Advanced carbonaceous materials for Zn-ion hybrid supercapacitors: status and perspectives. *Energy Materials* 5:500085

[23] Dong L, Ma X, Li Y, Zhao L, Liu W, et al. 2018. Extremely safe, high-rate and ultralong-life zinc-ion hybrid supercapacitors. *Energy Storage Materials* 13:96–102

[24] Wang C, Zeng C, Wei C, Chen G, Liang Y, et al. 2026. Lignin valorization towards porous carbon cathodes in zinc ion hybrid capacitors. *Chinese Chemical Letters* 37:111850
[25] Sun H, Liu C, Guo D, Liang S, Xie W, et al. 2022. P-doped porous carbon derived from walnut shell for zinc ion hybrid capacitors. *RSC Advances* 12:24724–24733
[26] Zhang H, Chen Z, Zhang Y, Ma Z, Zhang Y, et al. 2021. Boosting Zn-ion adsorption in cross-linked N/P co-incorporated porous carbon nanosheets for the zinc-ion hybrid capacitor. *Journal of Materials Chemistry A* 9:16565–16574
[27] Sun Z, Liao Y, Zhang Y, Sun S, Kan Q, et al. 2025. Sustainable carbon materials in environmental and energy applications. *Sustainable Carbon Materials* 1:e007
[28] Li Z, Wang C, Zeng C, Luo Y, Chen B, et al. 2026. *In-situ* synergistic activation engineering of nitrogen/oxygen co-doped gradient microporous carbons for high-rate zinc ion storage. *Chemical Engineering Science* 321:122969
[29] Zhang Y, Yu Z, Yue W, Zhang X, He T, et al. 2025. Formulation of N-doped carbon with meso/microporous structure for supercapacitors through biotemplates. *Journal of Industrial and Engineering Chemistry* 142:368–379
[30] Lai L, Zhao Y, Ying S, Li L, Ma Z, et al. 2018. Hierarchically porous N-doped carbon derived from supramolecular assembled polypyrrole as a high performance supercapacitor electrode material. *RSC Advances* 8:18714–18722
[31] Wang S, Qin J, Zhao Y, Duan L, Wang J, et al. 2019. Ultrahigh surface area N-doped hierarchically porous carbon for enhanced CO_2 capture and electrochemical energy storage. *ChemSusChem* 12:3541–3549
[32] Zhang L, Li G, Dong C, Jing L, Li Z, et al. 2020. Synthesis of rich N-doped hierarchically porous carbon flowers for electrochemical energy storage. *Diamond and Related Materials* 102:107691
[33] Daniel G, Kosmala T, Dalconi MC, Nodari L, Badocco D, et al. 2020. Upcycling of polyurethane into iron-nitrogen-carbon electrocatalysts active for oxygen reduction reaction. *Electrochimica Acta* 362:137200
[34] Song Y, Qu W, He Y, Yang H, Du M, et al. 2020. Synthesis and processing optimization of N-doped hierarchical porous carbon derived from corncob for high performance supercapacitors. *Journal of Energy Storage* 32:101877
[35] Ubaidullah M, Al-Enizi AM, Ahamad T, Shaikh SF, Al-Abdrabalnabi MA, et al. 2021. Fabrication of highly porous N-doped mesoporous carbon using waste polyethylene terephthalate bottle-based MOF-5 for high performance supercapacitor. *Journal of Energy Storage* 33:102125
[36] Calvo-Correas T, Ugarte L, Trzebiatowska PJ, Sanzberro R, Datta J, et al. 2017. Thermoplastic polyurethanes with glycolysate intermediates from polyurethane waste recycling. *Polymer Degradation and Stability* 144:411–419
[37] Cregut M, Bedas M, Durand MJ, Thouand G. 2013. New insights into polyurethane biodegradation and realistic prospects for the development of a sustainable waste recycling process. *Biotechnology Advances* 31:1634–1647
[38] Ahmad F, Cao W, Zhang Y, Pan R, Zhao W, et al. 2024. Oil recovery from microwave co-pyrolysis of polystyrene and polypropylene plastic particles for pollution mitigation. *Environmental Pollution* 356:124240
[39] Li Z, An Y, Dong S, Chen C, Wu L, et al. 2020. Progress on zinc ion hybrid supercapacitors: insights and challenges. *Energy Storage Materials* 31:252–266
[40] Ahmad F, Zhang Y, Liu Z, Zhao W, Liu W, et al. 2025. Aromatic enriched oil production via microwave-assisted catalytic co-pyrolysis of baked semen abutilon seeds and waste expanded polystyrene. *Journal of Cleaner Production* 528:146660
[41] Cao T, Li W, Zhu J, Zhang G, Liu H, et al. 2025. Transforming lignin into functionalized B/N co-doped porous carbon for high-performance zinc-ion hybrid capacitors. *Energy Conversion and Management* 326:119498
[42] Li H, Su P, Liao Q, Liu Y, Li Y, et al. 2023. Olive leaves-derived hierarchical porous carbon as cathode material for anti-self-discharge zinc-ion hybrid capacitor. *Small* 19:2304172
[43] Dang H, Xu R, Zhang J, Wang M, Xu K. 2023. Hydrothermal carbonization of waste furniture for clean blast furnace fuel production: physicochemical, gasification characteristics and conversion mechanism investigation. *Chemical Engineering Journal* 469:143980
[44] Liu Q, Xu R, Yan C, Han L, Lei H, et al. 2021. Fast hydrothermal co-liquefaction of corn stover and cow manure for biocrude and hydrochar production. *Bioresource Technology* 340:125630
[45] Liu Q, Ji G, Li X, Zhang G, Zhang X, et al. 2024. Insights into PVC-promoted hydrothermal carbonization of manure: dechlorination, inorganic metals removal, and combustion behaviors. *Chemical Engineering Journal* 491:152167
[46] Feng W, Feng N, Liu W, Cui Y, Chen C, et al. 2021. Liquid-state templates for constructing B, N, co-doping porous carbons with a boosting of potassium-ion storage performance. *Advanced Energy Materials* 11:2003215
[47] Wang H, Zhi L, Liu K, Dang L, Liu Z, et al. 2015. Thin-sheet carbon nanomesh with an excellent electrocapacitive performance. *Advanced Functional Materials* 25:5420–5427
[48] Zhang R, Jing X, Chu Y, Wang L, Kang W, et al. 2018. Nitrogen/oxygen co-doped monolithic carbon electrodes derived from melamine foam for high-performance supercapacitors. *Journal of Materials Chemistry A* 6:17730–17739
[49] Zhang Y, Wang X, Zou B, Xia B, Yang H, et al. 2025. Multidimensional soft-hard heterostructure porous carbon for high mass-loading zinc-ion hybrid supercapacitors. *Chemical Engineering Journal* 524:169366
[50] Wang B, Wang Y, Peng Y, Wang X, Wang N, et al. 2018. Nitrogen-doped biomass-based hierarchical porous carbon with large mesoporous volume for application in energy storage. *Chemical Engineering Journal* 348:850–859
[51] Shi X, Zhang H, Zeng S, Wang J, Cao X, et al. 2021. Pyrrolic-dominated nitrogen redox enhances reaction kinetics of pitch-derived carbon materials in aqueous zinc ion hybrid supercapacitors. *ACS Materials Letters* 3:1291–1299
[52] Yang L, Wu D, Wang T, Jia D. 2020. B/N-codoped carbon nanosheets derived from the self-assembly of chitosan–amino acid gels for greatly improved supercapacitor performances. *ACS Applied Materials & Interfaces* 12:18692–18704
[53] Chen W, Gong M, Li K, Xia M, Chen Z, et al. 2020. Insight into KOH activation mechanism during biomass pyrolysis: chemical reactions between O-containing groups and KOH. *Applied Energy* 278:115730
[54] Liu Y, Wu L. 2023. Recent advances of cathode materials for zinc-ion hybrid capacitors. *Nano Energy* 109:108290
[55] Fan Y, Fu F, Yang D, Liu W, Qiu X. 2024. Thiocyanogen-modulated N, S co-doped lignin hierarchical porous carbons for high-performance aqueous supercapacitors. *Journal of Colloid and Interface Science* 667:147–156
[56] Jian W, Zhang W, Wei X, Wu B, Liang W, et al. 2022. Engineering pore nanostructure of carbon cathodes for zinc ion hybrid supercapacitors. *Advanced Functional Materials* 32:2209914
[57] Jian W, Zhang W, Wu B, Wei X, Liang W, et al. 2022. Enzymatic hydrolysis lignin-derived porous carbons through ammonia activation: activation mechanism and charge storage mechanism. *ACS Applied Materials & Interfaces* 14:5425–5438
[58] Zhang W, Yin J, Jian W, Wu Y, Chen L, et al. 2022. Supermolecule-mediated defect engineering of porous carbons for zinc-ion hybrid capacitors. *Nano Energy* 103:107827
[59] Song T, Zhao Y, Chen C, Gui X, Wu X, et al. 2024. Recyclable NaCl template assisted preparation of N/O co-doped porous carbon for zinc-ion hybrid capacitor. *Journal of Energy Storage* 98:113148
[60] Koolen CD, Oveisi E, Zhang J, Li M, Safonova OV, et al. 2024. Low-temperature non-equilibrium synthesis of anisotropic multimetallic nanosurface alloys for electrochemical CO_2 reduction. *Nature Synthesis* 3:47–57
[61] Tang Y, Chen J, Mao Z, Roth C, Wang D. 2023. Highly N-doped carbon with low graphitic-N content as anode material for enhanced initial Coulombic efficiency of lithium-ion batteries. *Carbon Energy* 5:e257